Geomagnetic main field modeling with DMSP

P. Alken

National Geophysical Data Center, NOAA, Boulder, Colorado, USA

S. Maus

National Geophysical Data Center, NOAA, Boulder, Colorado, USA

H. Lühr

Helmholtz Centre Potsdam, GFZ, German Research Centre for Geosciences, Potsdam, Germany

R. Redmon

National Geophysical Data Center, NOAA, Boulder, Colorado, USA

F. Rich

Lincoln Laboratory, Massachusetts Institute of Technology, Lexington, Massachusetts, USA

B. Bowman

Space Environment Technologies, Pacific Palisades, CA, USA

S. O'Malley

Atmospheric and Environmental Research, Inc., Lexington, Massachusetts, USA

Abstract. The Defense Meteorological Satellite Program (DMSP) launches and maintains a network of satellites to monitor the meteorological, oceanographic, and solar-terrestrial physics environments. In the past decade, geomagnetic field modelers have focused much attention on magnetic measurements from missions such as CHAMP, Ørsted and SAC-C. With the completion of the CHAMP mission in 2010, there have been no satellite-based vector magnetic field measurements available for main field modeling. In this study, we calibrate the Special Sensor Magnetometer (SSM) instrument onboard DMSP to create a dataset suitable for main field modeling. These vector field measurements are calibrated to compute instrument timing shifts, scale factors, offsets, and non-orthogonality angles of the fluxgate magnetometer cores. Euler angles are then computed to determine the orientation of the vector magnetometer with respect to a local coordinate system. We fit a degree 15 main field model to the dataset and compare with the World Magnetic Model (WMM) and Ørsted scalar measurements. We call this model DMSP-MAG-1 and its coefficients and software are available for download at http://geomag.org/models/dmsp.html. Our results indicate that the DMSP dataset will be a valuable source for main field modeling for the years between CHAMP and the upcoming Swarm mission.

Patrick Alken, National Geophysical Data Center, NOAA E/GC1, 325 Broadway, Boulder, CO 80305-3328, USA. (patrick.alken@noaa.gov)

1. Introduction

Satellite derived geomagnetic field measurements from recent missions have facilitated the creation of magnetic field models with unprecedented accuracy. These models, in turn, are used in a vast number of different scientific and engineering applications. Low-degree models, such as the World Magnetic Model [*Maus et al.*, 2010a] and the International Geomagnetic Reference Field (IGRF) [*Finlay et al.*, 2010] are used in industry for navigation, orienting antennas and solar panels, and mineral exploration. Scientists subtract these models from geomagnetic data to uncover smaller-scale signatures caused by sources in the Earth's core, crust, and ionosphere. More sophisticated models include a crustal component up to high spherical harmonic degrees, as well as an external field to capture time-varying magnetospheric effects [*Sabaka et al.*, 2004; *Maus et al.*, 2006; *Olsen et al.*, 2006, 2009; *Lesur et al.*, 2008]. These models are invaluable in studying the spatial structure and time dependence of the Earth's core, crustal, ionospheric and magnetospheric fields.

While many geomagnetic field models include data recorded by ground observatories, the high accuracy at high spherical harmonic degrees would not be possible without satellite measurements. Many of these models are based on the past decade of measurements by the CHAMP [*Reigber et al.*, 2003], Ørsted [*Olsen et al.*, 2003], and SAC-C [*Colomb et al.*, 2004] satellites which have provided unprecedented spatial coverage of the geomagnetic field. Ørsted is the only one of these satellites still in orbit, however it has provided only scalar field measurements since 2004. Therefore, there have been no scientific-quality vector measurements of the geomagnetic field from satellites since the end of the CHAMP mission in September 2010. While the upcoming Swarm satellite mission [*Friis-Christensen et al.*, 2006] was originally scheduled to launch toward the end of CHAMP's mission life, delays have now created a multi-year gap in satellite vector measurements. Filling in this gap would provide a large benefit to studies of secular variation, ionospheric and magnetospheric effects, and main field modeling efforts in the post-CHAMP era.

In this study, we investigate the suitability of the fluxgate magnetometer onboard the Defense Meteorological Satellite Program (DMSP) satellites for main field modeling. The primary purpose of the DMSP satellites is for weather forecasting. Therefore, while they do carry vector magnetometers, the satellites were not designed to be as magnetically clean as the Ørsted, CHAMP, and upcoming Swarm missions. Early DMSP satellites (F-14 and prior) mounted their magnetometers on the body of the satellite leading to significantly higher noise in the magnetic field measurements. Starting with F-15, the magnetometer was mounted on a 5 meter boom assembly which greatly helped reduce the instrument noise and contamination from other spacecraft fields. In our study, we restrict our analysis to the spacecraft F-15 through F-18, which all have boom-mounted magnetometers.

In section 2 we discuss the DMSP fluxgate magnetometer instrument. Section 3 describes the calibration procedure for the vector magnetic measurements, including the timing shift, scalar calibration parameters, and Euler angles. In section 4 we fit a main field model to the calibrated dataset. Finally, in section 5 we validate our model against recent Ørsted scalar field measurements.

2. DMSP SSM Measurements

The observations used for this study were made by the special sensor magnetometer (SSM) instruments onboard the Defense Meteorological Satellite Program (DMSP) satellites F-15, F-16, F-17, and F-18. These DMSP satellites fly in sun-synchronous, polar orbits, with inclinations of about 98.8°, periods of about 102 minutes, and altitudes between 835 and 850 km [*Burke et al.*, 2011]. F-15 was launched in December 1999 into an orbit with ascending and descending nodes of about 21:10 and 09:10 LT, respectively. F-16 was launched in October 2003 into an orbit with ascending and descending nodes of about 20:01 and 08:01 LT. F-17 was launched in November 2006 with ascending and descending nodes near 17:32 and 05:32 LT. F-18 was launched in October 2009; its ascending and descending nodes are near 19:54 and 07:54 LT.

The SSM instruments are triaxial fluxgate magnetometers mounted on 5 meter booms and directed anti-radially (upward) from the spacecraft. They measure the geomagnetic field vector at a rate of 12 Hz and with a resolution of 2 nT. These vector measurements are then averaged over one second and provided as 1 Hz data in the spacecraft frame. The vector components of the SSM measurements are provided in a coordinate system which we assume to be unknown. We do however assume that this system is fixed with respect to the spacecraft, and using our knowledge of the attitude control system, we will define our own spacecraft-fixed coordinate system which will enable us to orient the measurements in a local geocentric frame. This is discussed in detail in the next section.

3. Magnetometer Calibration

Some initial calibration of the DMSP SSM data is performed by the Air Force prior to distributing the data publicly. Attempts are made to detect and remove large fields due to the magneto-torquers and instruments on the satellite. Additionally, scalar calibration is performed using the IGRF [*Finlay et al.*, 2010] as the reference field model. However, there continue to exist significant artifacts in the data, including frequent data jumps of 10-30 nT, and systematic large-scale structures which could have adverse effects on accurate main field modeling. Several examples of these effects are shown in Fig. 1. Here we plot scalar residuals from F-17 along a few orbits after subtracting the Pomme-8 main field model [*Maus et al.*, 2010b] for data recorded on 4 May 2011. Pomme-8 is a degree 133 main field model based on CHAMP measurements until 2010 and Ørsted measurements until 2013. It also includes an external field component [*Lühr and Maus*, 2010]. Specifically, the residual is calculated as

$$r = F_{ssm} - F_{int} - \hat{\mathbf{b}}_{int} \cdot \mathbf{B}_{ext} \tag{1}$$

where F_{ssm} is the scalar SSM measurement, $F_{int} = |\mathbf{B}_{int}|$ is the Pomme-8 scalar internal field up to degree 16, $\hat{\mathbf{b}}_{int} = \mathbf{B}_{int}/F_{int}$ is a unit vector in the main field direction, and $\mathbf{B}_{ext}$ is the Pomme-8 external field. Since we are subtracting scalar fields, we must project the external field onto the internal field direction. The data jumps in the figure are common features for all DMSP satellites and exist during nearly all orbits we have analyzed. They are likely due to other devices, such as heaters, turning on for several minutes and then shutting off, though we have not carefully tracked their origins due to a lack of availability of the satellites' housekeeping data. They are not thought to be due to the magneto-torquers, as these effects are removed from the dataset prior to public distribution. In addition to the data jumps, we see larger scale structure, particularly a prominent minimum in the residuals at low-latitudes and maxima at higher latitudes. These features could be due to remanent and/or induced magnetization of the spacecraft, or insufficiently calibrated data. Both the small and large-scale structure seen in the figure could have detrimental effects on attempts to create a main field model, and so it is necessary to carefully detect and remove these features from the data. Therefore, we have recalibrated the DMSP SSM measurements using a multi-step procedure, following the work of other satellite missions (e.g. [*Yin and Lühr*, 2011; *Le et al.*, 2011]), which performs both a scalar calibration and a vector calibration to recover the Euler angles required to analyze the data in a geocentric coordinate system.

A key step in calibrating and analyzing the DMSP SSM data lies in accurate orbital position determination. Since the DMSP satellites do not carry GPS receivers, their orbital positions are determined through radar tracking and orbital propagation. A differential orbit correction program is used to fit Space Surveillance Network (SSN) observations to obtain the standard 6 Keplerian elements plus the ballistic coefficient (B). The differential correction orbit fits are obtained using a weighted least squares approach that uses special perturbations orbit integration. The geopotential selected for use in the differential orbit corrections is the EGM96 [*Lemoine et al.*, 1998] model truncated to a 48×48 field. The special perturbation integration also includes third-body gravitational effects of the sun and moon, solar radiation pressure, earth and ocean tide effects, and accelerations due to atmospheric drag. The atmospheric density model used in the integration is a modified Jacchia [*Jacchia*, 1970] 1970 model that was developed for incorporation into the Air Force's High Accuracy Satellite Drag Model (HASDM) program [*Storz et al.*, 2002]. The modified Jacchia 1970 model uses the same Jacchia equations to compute the density but also incorporates additional equations to compute new temperature and density partial derivatives for improved orbit fits. The HASDM model processes drag information from the trajectories of 75 to 80 inactive payloads and debris (calibration satellites) to solve for a dynamically changing global correction to the thermospheric and exospheric neutral density. This correction covers the altitude range of 200 to 900 km. Satellite tracking observations (azimuth, elevation, range, and range rate) of the calibration satellites, obtained from the Space Surveillance Network, are processed directly to derive the neutral atmospheric density. Thermospheric density correction parameters are computed along with the trajectory states of the calibration satellites in a single estimation process, known as the Dynamic Calibration Atmosphere (DCA). DCA estimates 13 global density correction parameters. This global correction not only reduces the errors in the state error covariance for non-calibration satellites, but also makes these errors more realistic. An important feature of DCA is its segmented solution approach. Although the state vector of each calibration satellite is estimated for a 2-day fit span interval, the density correction parameters are estimated on 3-hour sub-intervals within the fit span. This approach is used to extract the time resolution needed to accurately determine the dynamically changing thermospheric density. This is especially important during geomagnetic storms, when the Joule heating and particle precipitation of the auroral ovals drive rapidly changing density features. However, to obtain this 3-hour resolution requires that the density parameters be constrained within the parameter solution. The constraints can be minimized though because of the large number (about 75 to 80) of calibration satellites used in the fits, and because of the heavy space surveillance sensor tasking which provides observations on almost every pass over almost every SSN sensor.

For non-calibration satellites such as DMSP the model also employs a segmented solution for the ballistic coefficient. This is a technique whereby an overall ballistic coefficient is estimated over the fit span and additional B type corrections are allowed to vary throughout the fit span. Fit spans of several days are divided into 100 minute segments for which a separate ballistic coefficient correction is estimated for each segment. This segment B technique is applied after the DCA density corrections are applied for each individual DMSP satellite, thus further improving the accuracy of the state vector estimate for the satellite trajectory. For DMSP satellites the SSN is heavily tasked to provide a radar track for every pass for every phased-array radar in the network. This provides very accurate radar observations on every single orbit. The orbit accuracy of the DMSP derived ephemeris has been estimated to have less than a 30m one standard deviation throughout the ephemeris.

3.1. Coordinate Systems

The DMSP attitude control system is designed to keep the Operational Linescan System (OLS) instrument aligned with the local geodetic vertical to within 0.01°. This essentially means we can define a satellite-fixed coordinate system using the local geodetic vertical direction, as well as the satellite's velocity vector. We define unit vectors in our satellite-fixed basis as

$$\hat{s}_1 = \frac{\mathbf{v}_t}{|\mathbf{v}_t|} \tag{2}$$

$$\hat{s}_2 = \hat{s}_3 \times \hat{s}_1 \tag{3}$$

$$\hat{s}_3 = -\hat{e}_\mu \tag{4}$$

where $\hat{e}_\mu$ is a unit vector in oblate spheroidal coordinates, which is outward normal to the local oblate spheroid defined by the WGS84 [*NIMA*, 2000] standard, and $\mathbf{v}_t = \mathbf{v} - (\mathbf{v} \cdot \hat{e}_\mu)\hat{e}_\mu$ is the component of the satellite velocity perpendicular to $\hat{e}_\mu$. With this definition, the basis vector $\hat{s}_3$ points in the downward local geodetic vertical direction, $\hat{s}_1$ points along the perpendicular velocity direction, and $\hat{s}_2$ completes the right-handed basis set. These basis vectors can be assumed to remain fixed with respect to the body of the satellite, up to the error in the attitude control system.

In our analysis, position and velocity vectors are transformed to Earth-Centered Inertial (ECI) coordinates, which represent standard Cartesian coordinates in a star-fixed frame centered at the Earth's center of mass. ECI coordinates provide a natural basis for solving the orbital equations which produce the DMSP positions and velocities, and they also greatly simplify the various calibration steps described below.

3.2. Data Selection

We process all available data from the DMSP F-15, F-16, F-17, and F-18 satellites from January 2009 through July 2013. In order to reduce unmodeled signals from external and ionospheric fields, we impose the following data selection criteria:

1. Dst index does not exceed 30 nT
2. Interplanetary Magnetic Field: $B_y \leq 2$ nT, $-2 \leq B_z \leq 6$ nT
3. Ap index less than 12 at mid/low latitudes ($\leq 60°$)
4. Ap index less than 27 at high-latitudes ($\geq 60°$)
5. Local times between 0630 and 1800 are excluded at mid/low latitudes ($\leq 60°$)
6. At high latitudes ($\geq 60°$), the sun must be at least 10° below the horizon to ensure darkness

3.3. Timing Shift

The first step in calibrating a satellite vector magnetometer is to compute its timing shift. This represents the delay between when a measurement is made by the instrument, and when it is given a timestamp and recorded. Due to the various electronics involved, this is typically on the order of several tens of milliseconds, which is significant for satellite measurements as the satellite moves by several hundred meters during this short time. Since the geomagnetic field can change by several nanotesla over this distance, it is important to accurately account for the timing shift for main field modeling. In order to calculate the timing shift, we calibrate the scalar measurements against a scalar reference field model. Specifically, we seek a time shift δt which minimizes the error function

$$\epsilon(\delta t) = \sum_i \left\{ F_i - F^{main}(\mathbf{r}(t_i + \delta t)) \right\}^2 \tag{5}$$

where t_i is the timestamp recorded with the scalar field measurement $F_i = |\mathbf{B}_i|$, F^{main} is the Pomme-8 scalar main field model, and $\mathbf{r}(t)$ is the satellite position at time t as given by the orbital propagation procedure discussed previously, and using Hermite polynomials to interpolate between the sampled points. Hermite polynomials have been shown to exhibit very small errors when interpolating orbit positions with sampling intervals of up to several minutes [*Korvenoja and Piche*, 2000].

The timing shift δt is calculated from Eq. (5) using 24 hours of data at a time and minimizing the error function using robust regression. Robust regression is used due to the high sensitivity of the timing shift calculation to data outliers as shown in Fig. 1. Robust regression is designed to reduce the effect of data outliers by assigning them small weights through iteration. While robust regression helps to counteract the effect of these data jumps, it cannot produce a long-term stable signal of the timing delay on its own, and so we have combined the timing shift calculation with the scalar calibration and outlier detection procedure discussed in the following sections.

3.4. Scalar Calibration Parameters

When a timing shift δt has been computed from Eq. (5), we compute the 9 vector magnetometer parameters common to all fluxgate instruments. These are 3 scale factors, 3 offsets and 3 non-orthogonality angles. The scale factors are typically linear proportionality parameters needed to convert the voltage readings of each magnetometer core into units of magnetic field. However, the DMSP SSM data has already undergone some calibration and is provided in units of magnetic field, and so our scale factors will be dimensionless quantities needed to bring the data into agreement with our scalar reference model. The 3 offsets represent the magnetic field reading of each magnetometer core if there is no current flowing through the coils. This can be due to remanent magnetization of the core material (or other nearby instruments on the satellite) as well as other sources of noise. Finally, the 3 non-orthogonality angles allow for the possibility that the 3 cores are slightly misaligned into a non-orthogonal coordinate system. These angles represent corrections designed to bring the 3 magnetometer axes into an orthogonal system. The equations relating the calibrated to the uncalibrated field components are discussed in detail in *Yin and Lühr* [2011] and *Lühr et al.* [2013] and are given below:

$$B_x = S_x E_x + O_x + E_y \cos \alpha_{xy} + E_z \cos \alpha_{xz} \tag{6}$$

$$B_y = S_y E_y + O_y + E_z \cos \alpha_{yz} \tag{7}$$

$$B_z = S_z E_z + O_z \tag{8}$$

Here, E_x, E_y, E_z represent the uncalibrated SSM field components in the spacecraft frame, S_x, S_y, S_z are the dimensionless scale factors, O_x, O_y, O_z are the offsets with units of nanotesla, and $\alpha_{xy}, \alpha_{xz}, \alpha_{yz}$ are the non-orthogonality angles. The vector $\mathbf{E}$ is provided by the Air Force in a spacecraft-fixed coordinate system which we are calling (x, y, z). Here, x points along the positive spacecraft velocity direction (approximately north/south), z points normal to the spacecraft and positive toward Earth (approximately downward), and y points normal to the orbital plane. The precise details of this coordinate system are not too important, since the timing and scalar calibration require only the scalar magnitude of the field vector, and the Euler angles will be computed using our own satellite-fixed basis $\hat{s}_1, \hat{s}_2, \hat{s}_3$. The scale factors, offsets, and non-orthogonality angles however are referenced to this coordinate system and so an approximate idea of the axis directions is useful in interpreting their values.

The scale factors, offsets and non-orthogonality angles are determined by comparing the scalar magnitude of the calibrated vector (B_x, B_y, B_z) with a known scalar reference model over a period of 24 hours of data. Setting $F_{cal}^2 = B_x^2 + B_y^2 + B_z^2$, we can define an error function

$$\epsilon(\mathbf{S}, \mathbf{O}, \alpha) = \sum_i \left\{ F_{cal}(\mathbf{S}, \mathbf{O}, \alpha; \mathbf{E}_i) - F^{main}(\mathbf{r}(t_i + \delta t)) \right\}^2 \qquad (9)$$

where $\mathbf{E}_i$ is the SSM vector measurement and δt is the previously computed timing shift. The scale factors, offsets, and non-orthogonality angles are recovered from Eq. (9) for each 24 hour period using nonlinear least squares regression. While only the scalar magnitude of the calibrated field vector is used in the least-squares inversion, unique solutions for the scale factors, offsets and non-orthogonality angles are guaranteed by using 24 hour periods of data, representing many orbits over which the magnetometer is rotated into many spatial orientations.

3.5. Outlier Detection

As mentioned in Sec. 3.3, data outliers can significantly influence the timing shift calculation, and this is also true for the 9 scalar calibration parameters discussed above. During a typical DMSP orbit, there can be between 5 and 10 large data jumps (as seen in Fig. 1). It is important to accurately detect and remove these effects from the data in order to produce reliable long-term signals of the timing shift and scalar calibration parameters.

Detecting these data jumps can be a challenging problem, especially during a first pass of the uncalibrated data where there can be significant structure in the residuals which tends to hide some of the outliers. Therefore, we use an iterative scheme, in which we select a 24 hour period of data, calculate a timing shift, calculate the scalar calibration parameters, and then detect and flag outliers in the calibrated data. Flagged outliers are then removed from subsequent iterations. The idea is that during each iteration, the calibrated residuals tend closer and closer to 0, making the data jumps more obvious and easier to detect.

The method we use for outlier detection is to first separate the 24 hour period of data into north and south flying half-orbit tracks. For each track, we fit a degree 5 polynomial to the scalar residuals as a function of latitude using robust regression to attempt to exclude the outliers. This polynomial is then subtracted from the residuals, and any remaining data point larger than 3 residual standard deviations is considered an outlier and flagged.

The iterative procedure is outlined below:

1. Select a 24 hour period of SSM measurements

2. For iteration k, compute a timing shift from this data using the procedure discussed in Sec. 3.3, ignoring any flagged outliers.

3. Using the timing shift from the previous step, calculate the 9 scalar calibration parameters as outlined in Sec. 3.4.

4. Fit and subtract a degree 5 polynomial in latitude to the calibrated scalar residuals using robust regression and flag any data points larger than 3 standard deviations.

5. Iterate steps 2-4 until no more outliers are detected

This procedure typically converges in about 5 iterations and works very well for the majority of orbital tracks, but it is not 100% accurate in detecting all data outliers. Problems can arise if there are exceptionally long baseline offsets (lasting many minutes) or if there are jumps near the poles where we select the beginning and end of our orbital tracks. In some of these cases, the polynomial fit to the residuals will be poor which can be detected and used to throw away the entire track. But other cases cannot be so easily detected. However, overall this procedure works quite well in producing reliable long-term signals of the timing shift and scalar calibration parameters. Figure 2 demonstrates the calibration and outlier iteration procedure discussed above. Each column of the figure contains a single latitudinal profile recorded by F-16 on 1 December 2010. The top row shows the two profiles after subtracting Pomme-8, computing an initial timing shift and scalar calibration, and computing a robust polynomial fit to the residuals. The middle row shows the result of subtracting the robust polynomial from the residuals, computing the standard deviation σ of the resulting data, and plotting $\pm 3\sigma$ lines. Data points outside of these lines are flagged as outliers and removed from further processing. The profiles are then iterated several more times until no further outliers are detected. The bottom row of the figure shows the final scalar residuals, after removing all outliers and computing and applying final timing shift and scalar calibration parameters. We see that the residual profile in the right column has been significantly flattened over the course of the calibration procedure. This is primarily due to the scalar calibration procedure discussed in Section 3.4, and indicates that the original DMSP data were not fully calibrated, leading to minima features at low-latitudes.

Figure 3 shows the final timing shift signal for all 4 satellites. We see significant day-to-day variability, which is likely due to the noise in the dataset, and occasionally could result from a failure to detect all outliers as previously discussed. In addition to the day-to-day variability, we see longer term trends which vary on timescales of a year or more. These are most likely due to thermal noise relating to the amount of sunlight and heat absorbed by the satellite throughout the year. Since these longer-term trends are clearly visible in the signals, we cannot simply use a mean value for the instrument timing. We therefore fit a smoothing spline to the signal for each satellite, shown in red in Fig. 3 in order to eliminate the effects of the short term variability. This smoothing spline is used as the final timing shift.

Figure 4 shows the scalar calibration signals for all 4 satellites. In the first column we plot the scale factors, which are dimensionless since the DMSP SSM measurements are already provided in units of nanotesla. We see that the X and Z scale factors are relatively low-noise and stable over the entire time period. This is because the X and Z directions are roughly equal to the northward and downward directions respectively, the strongest components of the geomagnetic field, and so are well resolved in the least-squares inversion. The Y component on the other hand, which is approximately eastward, represents the weakest component of the geomagnetic field over the orbit, and is less well constrained during the inversion. Therefore we find significant day-to-day noise in this component. The offsets are shown in the middle column and again show relative stability in the X and Z components and higher noise in the Y component. A nice secondary benefit of accurately determining the offsets is the removal of remanent magnetization fields. Since the offsets represent a constant field in the satellite frame, effects of remanent magnetization of materials close to the SSM instrument will be included and thus calibrated out of the data. The non-orthogonality angles are plotted in the last column. Here we see that the angles defined with respect to the poorly-resolved Y axis are noisier than α_{xz}, which measures the angle between the well-resolved X and Z magnetometer axes. In some of the scalar calibration curves we see a significant annual oscillation. We again attribute this to thermal noise related to the amount of sunlight and heat absorbed by the satellite as the Earth orbits the Sun throughout the year. By accurately determining the scalar calibration parameters for each satellite, these thermal effects will be removed from the dataset. We fit smoothing splines (not shown) to each scalar calibration parameter similar to the timing signals in order to eliminate the day-to-day noise and keep the longer-term trends in the signals.

3.6. Euler Angles

After the timing shift and scalar calibration parameters have been calculated, three Euler angles are computed which rotate the field vector into the spacecraft frame defined by the basis $\hat{s}_1, \hat{s}_2, \hat{s}_3$. The DMSP SSM data are already provided in a coordinate system fixed with respect to the satellite (up to errors in the attitude control system), and so we assume a constant three dimensional rotation from the provided coordinate system to our spacecraft basis. This rotation is defined by three Euler angles α, β, γ and the rotation is given by

$$\mathbf{B}^{\hat{s}}(\alpha, \beta, \gamma) = R_x(\alpha) R_y(\beta) R_z(\gamma) \mathbf{B}^{ssm} \tag{10}$$

where $\mathbf{B}^{ssm}$ is the calibrated magnetic field vector in some arbitrary spacecraft-fixed coordinate system, $\mathbf{B}^{\hat{s}}$ is the vector in the $\hat{s}_1, \hat{s}_2, \hat{s}_3$ basis, and the rotation matrices R_x, R_y, R_z represent rotations around the three coordinate axes of the arbitrary spacecraft-fixed system. Once we have the components of the magnetic field in the $\hat{s}_1, \hat{s}_2, \hat{s}_3$ basis, we may then transform them to geocentric coordinates:

$$\mathbf{B}^{geocentric}(\alpha, \beta, \gamma) = T \mathbf{B}^{\hat{s}}(\alpha, \beta, \gamma) \tag{11}$$

where the transformation matrix T is given by

$$T = \begin{pmatrix} \hat{r} \cdot \hat{s}_1 & \hat{r} \cdot \hat{s}_2 & \hat{r} \cdot \hat{s}_3 \\ \hat{\theta} \cdot \hat{s}_1 & \hat{\theta} \cdot \hat{s}_2 & \hat{\theta} \cdot \hat{s}_3 \\ \hat{\phi} \cdot \hat{s}_1 & \hat{\phi} \cdot \hat{s}_2 & \hat{\phi} \cdot \hat{s}_3 \end{pmatrix} \tag{12}$$

and $\hat{r}, \hat{\theta}, \hat{\phi}$ are the standard geocentric spherical basis vectors and $\hat{s}_1, \hat{s}_2, \hat{s}_3$ are given in Eqs. 2-4. The unknown Euler angles α, β, γ are then computed by minimizing the error function

$$\epsilon(\alpha, \beta, \gamma) = \sum_i \left\{ \mathbf{B}_i^{geocentric}(\alpha, \beta, \gamma) - \mathbf{B}^{main}(\mathbf{r}(t_i + \delta t)) \right\}^2 \tag{13}$$

where $\mathbf{B}_i^{geocentric}$ is the ith vector measurement transformed into geocentric coordinates using the Euler angles α, β, γ, and $\mathbf{B}^{main}$ is the Pomme-8 vector field model. Euler angles are computed for each 24-hour time period, and time series of α, β, γ are shown in Fig. 5 for each of the DMSP satellites.

3.7. Final Calibrated Residuals

Figure 6 shows the scalar residuals for F-16 taking all data for 2010, binning it in latitude and longitude and averaging each bin. We select 2010 since that was the last year of CHAMP vector measurements and so the Pomme-8 model is more accurate during that time frame. The left panel shows the original, uncalibrated data after subtracting Pomme-8. We see here the distinctive band of minima at low-latitudes, seen earlier in Fig. 1. The residuals are on the order of 80 nT, which is far too large for accurate main field modeling. In the right panel we show the same dataset after performing the timing, scalar, and Euler angle calibration, and eliminating outliers. Here we plot the dataset on the same 80 nT scale, but the residuals are in fact closer to 10 nT. Additionally, the systematic structure at low-latitudes has largely disappeared as a result of the calibration.

Figure 7 shows the calibrated scalar residuals for all satellites F-15 through F-18 for the years 2009-2013, plotted on a scale of 10 nT. For each year, the data are binned in latitude and longitude and averaged over the year. Figure 8 shows the downward component calibrated B_z residuals for the same years. These are on the order of 30 nT for 2009-2011 and get larger in the later years 2012-2013. This is because the Pomme-8 model used to calibrate the dataset is primarily based on CHAMP measurements and therefore cannot accurately predict the secular variation after 2010.

4. Main Field Modeling

Next we fit a spherical harmonic degree 15 main field model to the calibrated DMSP dataset. The model is given by

$$B_x = \sum_{nm} \left(\frac{a}{r}\right)^{n+2} \left(g_{nm}(t)\cos m\phi + h_{nm}(t)\sin m\phi\right) \frac{\partial}{\partial\theta} P_{nm}(\cos\theta) \tag{14}$$

$$B_y = \frac{1}{\sin\theta} \sum_{nm} \left(\frac{a}{r}\right)^{n+2} m \left(g_{nm}(t)\sin m\phi - h_{nm}(t)\cos m\phi\right) P_{nm}(\cos\theta) \tag{15}$$

$$B_z = -\sum_{nm} (n+1) \left(\frac{a}{r}\right)^{n+2} \left(g_{nm}(t)\cos m\phi + h_{nm}(t)\sin m\phi\right) P_{nm}(\cos\theta) \tag{16}$$

where the degree n is summed from 1 to 15, order m is summed from 0 to n, r, θ, ϕ are the standard geocentric spherical coordinates, $P_{nm}(\cos\theta)$ is the Schmidt semi-normalized associated Legendre function, a is the geomagnetic reference radius (6371.2 km), and the time-dependent coefficients are given by

$$g_{nm}(t) = g_{nm}^0 + \dot{g}_{nm}(t - t_0) + \frac{1}{2}\ddot{g}_{nm}(t - t_0)^2 \tag{17}$$

$$h_{nm}(t) = h_{nm}^0 + \dot{h}_{nm}(t - t_0) + \frac{1}{2}\ddot{h}_{nm}(t - t_0)^2 \tag{18}$$

with the main field coefficients g_{nm}^0, h_{nm}^0, secular variation coefficients $\dot{g}_{nm}, \dot{h}_{nm}$, and secular acceleration coefficients $\ddot{g}_{nm}, \ddot{h}_{nm}$ to be determined. The epoch t_0 was chosen as 2012.0. The unknown coefficients are computed through robust linear regression using all calibrated DMSP data from 2010.5 through 2013.5. A three year period was chosen since the model's time dependence is represented by a quadratic polynomial and three years of data were found to be long enough to accurately determine the secular acceleration. Only the vertical B_z component and scalar magnitude of the DMSP data were used for the modeling, since the B_x and B_y components are highly influenced by ionospheric and magnetospheric currents at high-latitudes. The B_z component is also influenced to a lesser extent by these systems, however it is required to include this in the modeling since the scalar data alone cannot guarantee a unique solution [*Backus*, 1986]. Therefore, we use the B_z component data only below 55 degrees latitude to minimize the influence of high-latitude currents, and use the scalar data at all latitudes.

Since the polar regions are sampled much more frequently than mid and low-latitudes, we organize the data into 1.8° latitude by 3.6° longitude bins and assign initial weights to the data as

$$w_{ij} = \frac{1}{K}\sqrt{\frac{a_{ij}}{n_{ij}}} \qquad (19)$$

where a_{ij}, n_{ij} are the area on a unit sphere and number of measurements for bin (i, j), respectively. These are designed to upweight sparsely sampled regions with larger areas (typically low-latitudes) and downweight densely sampled regions with smaller areas (typically at the poles). K is a normalization constant chosen so that $\sum_{ij} w_{ij} = 1$. Applying these weights to the data significantly reduces the condition number of the least squares matrix and improves the resulting solution.

Further reduction of the matrix condition number was achieved by nondimensionalizing the time dependent factors $t - t_0$ in the model and applying Tikhonov regularization [*Tikhonov et al.*, 1995] to the secular acceleration coefficients above degree 8. Damping these coefficients helps to mitigate the effect of the polar data gap due to DMSP's inclination of 98.8°.

Additional weighting factors are computed via iteratively reweighted least squares (IRLS) using the Huber weighting function [*Huber*, 1996]. At each step of the iteration, these Huber weights are multiplied by the initial weights in Eq. 19 to produce the final weights. This procedure helps to minimize the effect of data outliers on the final model. The system is iterated 5 times to achieve convergence. The condition number of the final least squares matrix was 49.6 and the corresponding eigenvalue spectrum is shown in Fig. 9. We see here that the spectrum decreases relatively smoothly with coefficient index, indicating that the secular variation and acceleration coefficients are well resolved in the model. We call the resulting model DMSP-MAG-1 and its coefficients and software are available on the web at http://geomag.org/models/dmsp.html.

4.1. External field

We include a simple model of fields originating in the magnetosphere and their induced counterparts. Here, we allow for an external field aligned with the dipole component of the main field, in addition to the steady ring current. The field can be represented as

$$\mathbf{B}_{ext} = RC + E_{st} \sum_{m=0}^{1} \begin{bmatrix} \left(\tilde{g}_{1m} \cos m\phi + \tilde{h}_{1m} \sin m\phi\right) \partial_\theta P_{1m} \\ \frac{m}{\sin\theta} \left(\tilde{g}_{1m} \sin m\phi - \tilde{h}_{1m} \cos m\phi\right) P_{1m} \\ \left(\tilde{g}_{1m} \cos m\phi + \tilde{h}_{1m} \sin m\phi\right) P_{1m} \end{bmatrix} +$$

$$I_{st} \left(\frac{a}{r}\right)^3 \sum_{m=0}^{1} \begin{bmatrix} \left(\tilde{g}_{1m} \cos m\phi + \tilde{h}_{1m} \sin m\phi\right) \partial_\theta P_{1m} \\ \frac{m}{\sin\theta} \left(\tilde{g}_{1m} \sin m\phi - \tilde{h}_{1m} \cos m\phi\right) P_{1m} \\ -2 \left(\tilde{g}_{1m} \cos m\phi + \tilde{h}_{1m} \sin m\phi\right) P_{1m} \end{bmatrix} \tag{20}$$

where $(\tilde{g}_{10}, \tilde{g}_{11}, \tilde{h}_{11}) = \frac{1}{\sqrt{g_{10}^2 + g_{11}^2 + h_{11}^2}} (g_{10}, g_{11}, h_{11})$ are the normalized main field dipole coefficients computed previously, E_{st} and I_{st} are the external and induced components of the external dipole field aligned with the main field [*Maus and Weidelt*, 2004], and RC represents the steady ring current field. The term RC is also a degree 1 spherical harmonic expansion of the external field, whose coefficients we took from Pomme-8. The above external field model offers a first-order approximation to the true external field, since a more sophisticated model would separate the contributions of the inner and outer magnetosphere into solar-magnetic (SM) and geocentric-solar-magnetospheric (GSM) coordinates [*Maus and Lühr*, 2005; *Lühr and Maus*, 2010].

5. Validation

We perform two validations of the model DMSP-MAG-1. The first is to compare with the World Magnetic Model (WMM) 2010 [*Maus et al.*, 2010a]. WMM2010 is a degree 12 main field model based on data from CHAMP, Ørsted, and ground magnetic observatories prior to and including 2010. In order to make a realistic comparison, we recalculated a DMSP-based model using data from 2009-2011 and using the same epoch $t_0 = 2010.0$ as the WMM2010. Figure 10 shows the main field and secular variation spectra for the two models, as well as the secular acceleration of DMSP-MAG-1. The main field coefficients agree very well while the secular variation exhibits small differences above spherical harmonic degree 9. This could be due to the polar data gap in the DMSP dataset.

Next, we compare DMSP-MAG-1 with recent Ørsted satellite scalar data. We selected all available Ørsted data from January to June 2013 using the same data selection criteria discussed in section 3.2. Then we constructed a model based on the DMSP satellites from January 2010 through July 2013. The residuals were binned in latitude and longitude and averaged, and are shown in Fig. 11 (right). For comparison, we also show the Ørsted residuals against WMM2010 in the left panel. We can see that the DMSP residuals are significantly smaller than the WMM2010 for 2013. The rms difference over the globe is 11.4 nT for DMSP, and 20.8 nT for WMM2010.

6. Conclusion

We have calibrated the vector fluxgate magnetometer instruments on the DMSP F-15, F-16, F-17 and F-18 satellites to obtain a dataset suitable for main field modeling in the post-CHAMP era. First, careful orbit determination was performed to yield ephemeris accurate to within 30m at one standard deviation over the orbit. Next, we calculated the instruments' timing shifts, scalar calibration parameters, and Euler angles, in addition to carefully detecting and removing outliers due to other spacecraft fields. The resulting calibrated dataset, when compared with Pomme-8, has rms scalar residuals of about 10 nT and rms B_z residuals of about 30 nT. We fit a degree 15 main field model to the calibrated DMSP dataset and find good agreement with WMM2010 during the years 2009-2011. When compared with recent Ørsted scalar measurements, our DMSP-MAG-1 model offers a significant improvement over WMM2010, yielding rms differences of about 11 nT, compared with 21 nT for WMM2010. We believe this dataset will offer a valuable source of vector geomagnetic measurements in the years between CHAMP and the upcoming Swarm mission.

Acknowledgments. The DMSP magnetometer data are publicly available from the NOAA National Geophysical Data Center (NGDC) through arrangement with the Air Force Research Laboratory (AFRL) and the Defense Meteorological Satellite Program (DMSP). The CHAMP mission was sponsored by the Space Agency of the German Aerospace Center (DLR) through funds of the Federal Ministry of Economics and Technology. The Ørsted Project was made possible by extensive support from the Ministry of Trade and Industry, the Ministry of Research and Information Technology and the Ministry of Transport in Denmark.

References

Backus, G. (1986), Poloidal and toroidal fields in geomagnetic field modeling, *Rev. Geophys.*, *24*(1), 75–109.

Burke, W. J., G. R. Wilson, C. S. Lin, F. J. Rich, J. O. Wise, and M. P. Hagan (2011), Estimating Dst indices and exospheric temperatures from equatorial magnetic fields measured by DMSP satellites, *J. Geophys. Res.*, *116*, A01205, doi:10.1029/2010JA015310.

Colomb, F. R., C. Alonso, C. Hofmann, and I. Nollmann (2004), SAC-C mission, an example of international cooperation, *Advances in Space Research*, *34*(10), 2194–2199, doi:10.1016/j.asr.2003.10.039.

Finlay, C. C., et al. (2010), International Geomagnetic Reference Field: The Eleventh Generation, *Geophys. J. Int.*, *183*, 1216–1230, doi:10.1111/j.1365-246X.2010.04804.x, Issue 3.

Friis-Christensen, E., H. Lühr, and G. Hulot (2006), Swarm: A constellation to study the Earth's magnetic field, *Earth Planets Space*, *58*, 351–358.

Huber, P. J. (1996), *Robust Statistical Procedures*, CBMS-NSF Regional Conference Series in Applied Mathematics, Society for Industrial and Applied Mathematics.

Jacchia, L. G. (1970), New Static Models of the Thermosphere and Exosphere with Empirical Temperature Profiles, *Smithson. Astrophys. Obs. Special Report*, *313*.

Korvenoja, P., and R. Piche (2000), Efficient satellite orbit approximation, in *Proceedings of the 13th International Technical Meeting of the Satellite Division of The Institute of Navigation (ION GPS 2000)*, pp. 1930–1937, Salt Lake City, UT.

Le, G., W. J. Burke, R. F. Pfaff, H. T. Freudenreich, S. Maus, and H. Lühr (2011), C/NOFS measurements of magnetic perturbations in the low-latitude ionosphere during magnetic storms, *J. Geophys. Res.*, *116*, A12230, doi:10.1029/2011JA017026.

Lemoine, F. G., et al. (1998), The Development of the Joint NASA GSFC and NIMA Geopotential Model EGM96, NASA/TP-1998-206861.

Lesur, V., I. Wardinski, M. Rother, and M. Mandea (2008), GRIMM: the GFZ Reference Internal Magnetic Model based on vector satellite and observatory data, *Geophys. J. Int.*, *173*, 382–394, doi:10.1111/j.1365-246X.2008.03724.x.

Lühr, H., and S. Maus (2010), Solar cycle dependence of quiet-time magnetospheric currents and a model of their near-Earth magnetic fields, *Earth Planets Space*, *62*, 843–848.

Lühr, H., F. Yin, and R. Bock (2013), Magnetic properties of CHAMP and their effects on in-orbit calibration, *J. Sens. Sens. Syst.*, *2*, 9–17, doi:10.5194/jsss-2-9-2013.

Maus, S., and H. Lühr (2005), Signature of the quiet-time magnetospheric magnetic field and its electromagnetic induction in the rotating Earth, *Geophys. J. Int.*, *162*, 755–763, doi:10.1111/j.1365-246X.2005.02691.x.

Maus, S., and P. Weidelt (2004), Separating the magnetospheric disturbance magnetic field into external and transient internal contributions using a 1D conductivity model of the Earth, *Geophys. Res. Lett.*, *31*, L12614, doi:10.1029/2004GL020232.

Maus, S., M. Rother, C. Stolle, W. Mai, S. Choi, H. Lühr, D. Cooke, and C. Roth (2006), Third generation of the Potsdam Magnetic Model of the Earth (POMME), *Geochem. Geophys. Geosyst.*, *7*, doi:10.1029/2006GC001269.

Maus, S., S. Macmillan, S. McLean, B. Hamilton, A. Thomson, M. Nair, and C. Rollins (2010a), The US/UK World Magnetic Model for 2010-2015, *NOAA Technical Report NESDIS/NGDC*.

Maus, S., C. Manoj, J. Rauberg, I. Michaelis, and H. Lühr (2010b), NOAA/NGDC candidate models for the 11th generation International Geomagnetic Reference Field and the concurrent release of the 6th generation Pomme magnetic model, *Earth Planets Space*, *62*, 729–735.

NIMA (2000), Department of Defense World Geodetic System 1984, Its Definition and Relationships With Local Geodetic Systems, *Tech. Rep. TR8350.2*, National Imagery and Mapping Agency, Third edition.

Olsen, N., H. Lühr, T. J. Sabaka, M. Mandea, M. Rother, L. Tøffner-Clausen, and S. Choi (2006), CHAOS - a model of the Earth's magnetic field derived from CHAMP, Ørsted, and SAC-C magnetic satellite data, *Geophys. J. Int.*, *166*(1), 67–75, doi:10.1111/j.1365-246X.2006.02959.x.

Olsen, N., M. Mandea, T. J. Sabaka, and L. Tøffner-Clausen (2009), CHAOS-2 - a geomagnetic field model derived from one decade of continuous satellite data, *Geophys. J. Int.*, *179*(3), 1477–1487, doi:10.1111/j.1365-246X.2009.04386.x.

Olsen, N., et al. (2003), Calibration of the Ørsted Vector Magnetometer, *Earth Planets Space*, *55*, 11–18.

Reigber, C., H. Lühr, and P. Schwintzer (2003), *First CHAMP Mission Results for Gravity, Magnetic and Atmospheric Studies*, Springer.

Sabaka, T. J., N. Olsen, and M. E. Purucker (2004), Extending comprehensive models of the Earth's magnetic field with Ørsted and CHAMP data, *Geophys. J. Int.*, *159*, 521–547, doi:10.1111/j.1365-246X.2004.02421.x.

Storz, M., B. R. Bowman, and J. I. Branson (2002), High Accuracy Satellite Drag Model (HASDM), in *AIAA/AAS Astrodynamics Specialist Conference*, Monterey, California, AIAA-2002-4886.

Tikhonov, A., A. Goncharsky, V. Stepanov, and A. G. Yagola (1995), *Numerical Methods for the Solution of Ill-Posed Problems*, Mathematics and Its Applications, Springer.

Yin, F., and H. Lühr (2011), Recalibration of the CHAMP satellite magnetic field measurements, *Measurement Science and Technology*, *22*(5), doi:10.1088/0957-0233/22/5/055101.

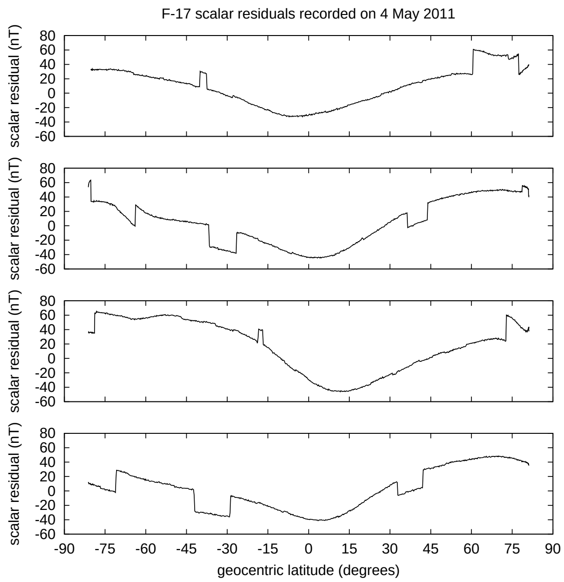

Figure 1. Samples of DMSP scalar residuals after subtracting Pomme main field model for several orbital tracks. Data were recorded by F-17 on 4 May 2011.

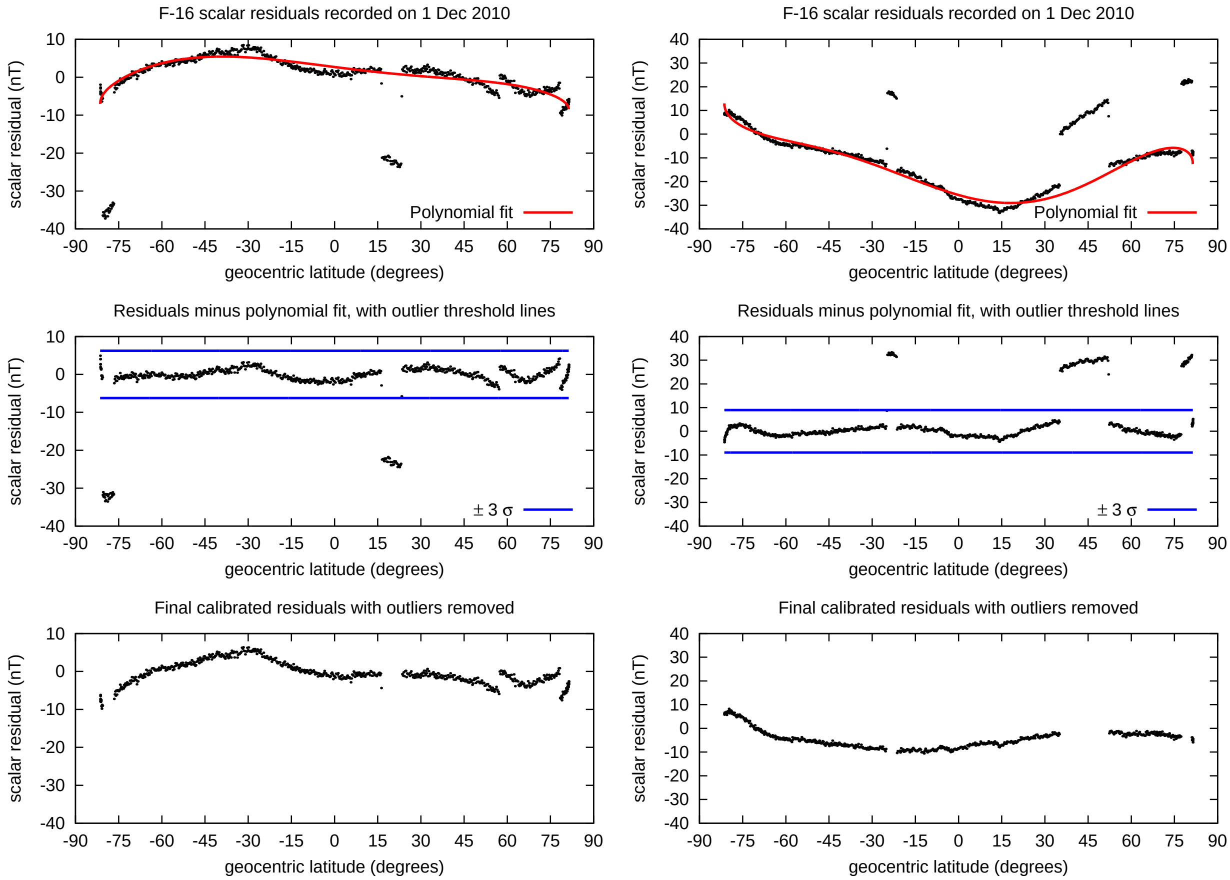

Figure 2. Each column contains an example of a magnetic profile with outlier detection iteration. Top: uncalibrated scalar residual after subtracting Pomme model (black) with robust polynomial fit (red). Middle: uncalibrated scalar residual minus robust polynomial (black) with $\pm 3\sigma$ lines (blue) to detect outliers. Bottom: final residual after applying timing shift and scalar calibration and eliminating outliers. These data were recorded by F-16 during two separate orbits on 1 December 2010.

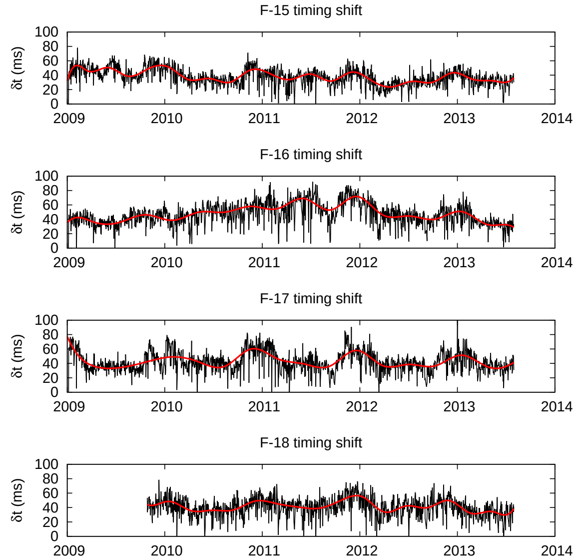

Figure 3. Timing shift time series (black) for DMSP satellites from January 2009 through July 2013, except for F-18 which was launched in October 2009. Red curves show smoothing splines used for final timing signal.

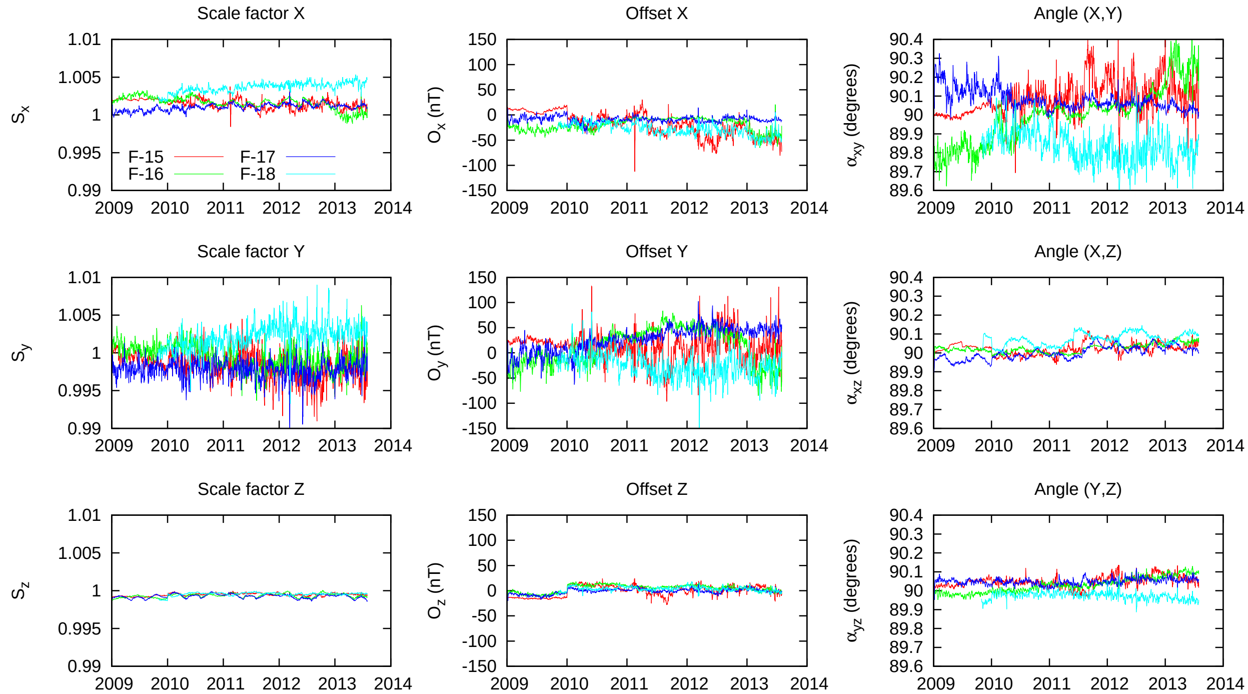

Figure 4. Scale factors, offsets, and non-orthogonality angles for F-15 (red), F-16 (green), F-17 (blue), and F-18 (teal). Smoothing splines are fitted to each parameter (not shown).

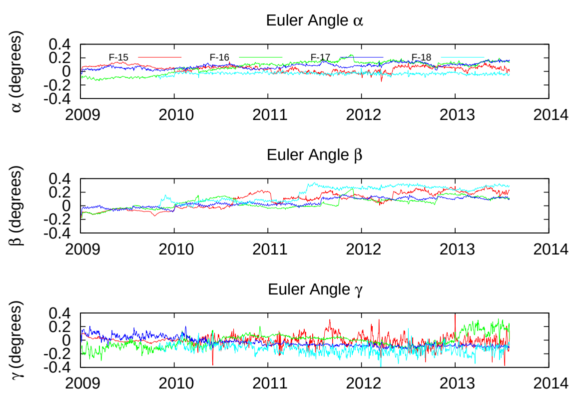

Figure 5. Euler angles computed daily from each DMSP satellite. Smoothing splines are fitted to each parameter (not shown).

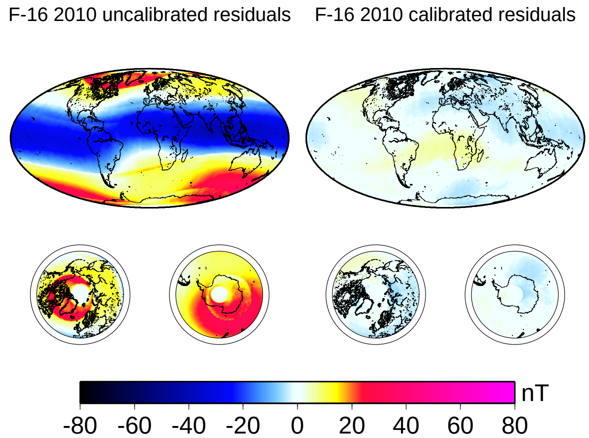

Figure 6. Pomme-8 scalar residuals for F-16 averaged over 2010 gridded in latitude and longitude prior to calibration (left) and after calibration (right).

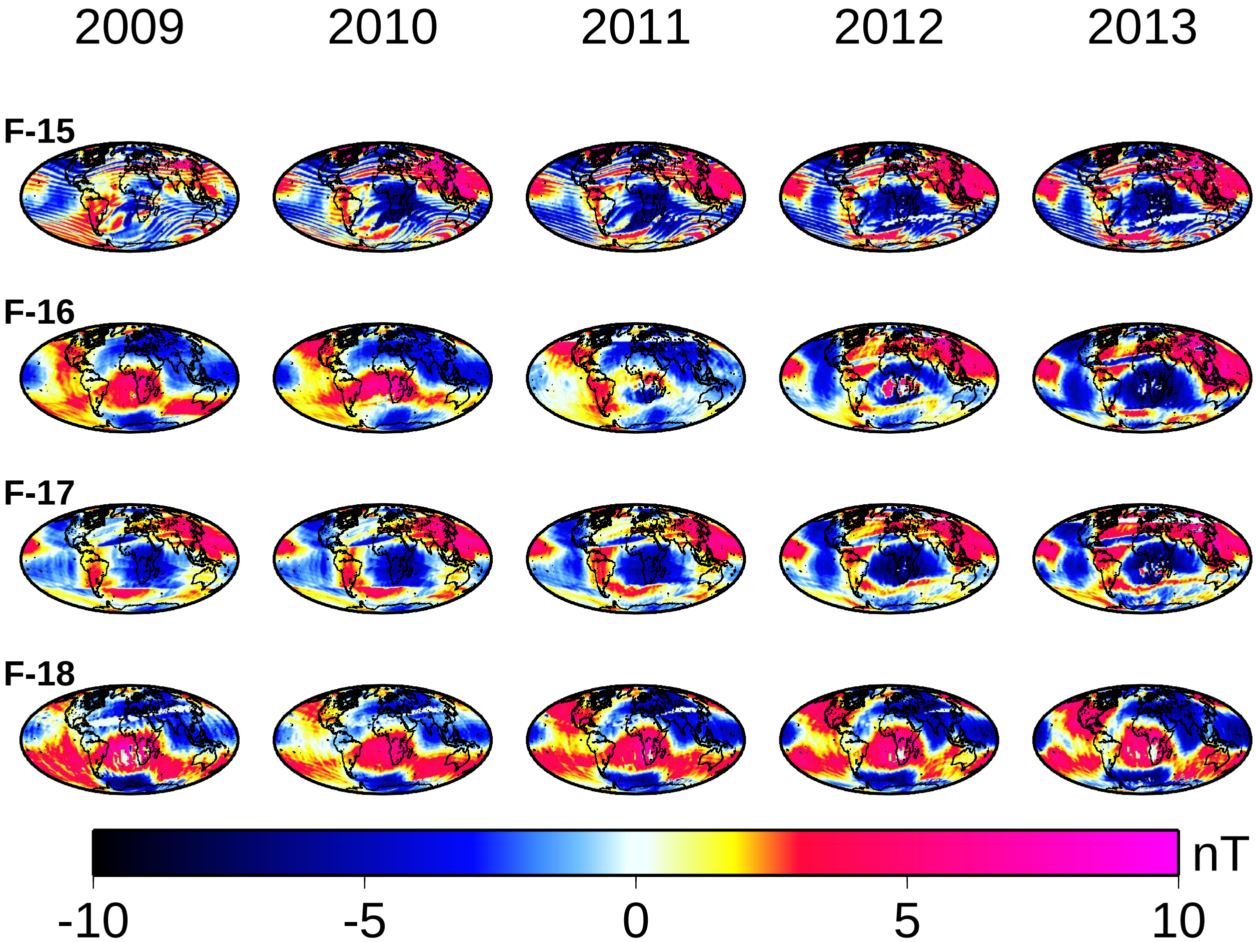

Figure 7. Calibrated scalar residuals for all satellites F-15 through F-18 and years 2009-2013.

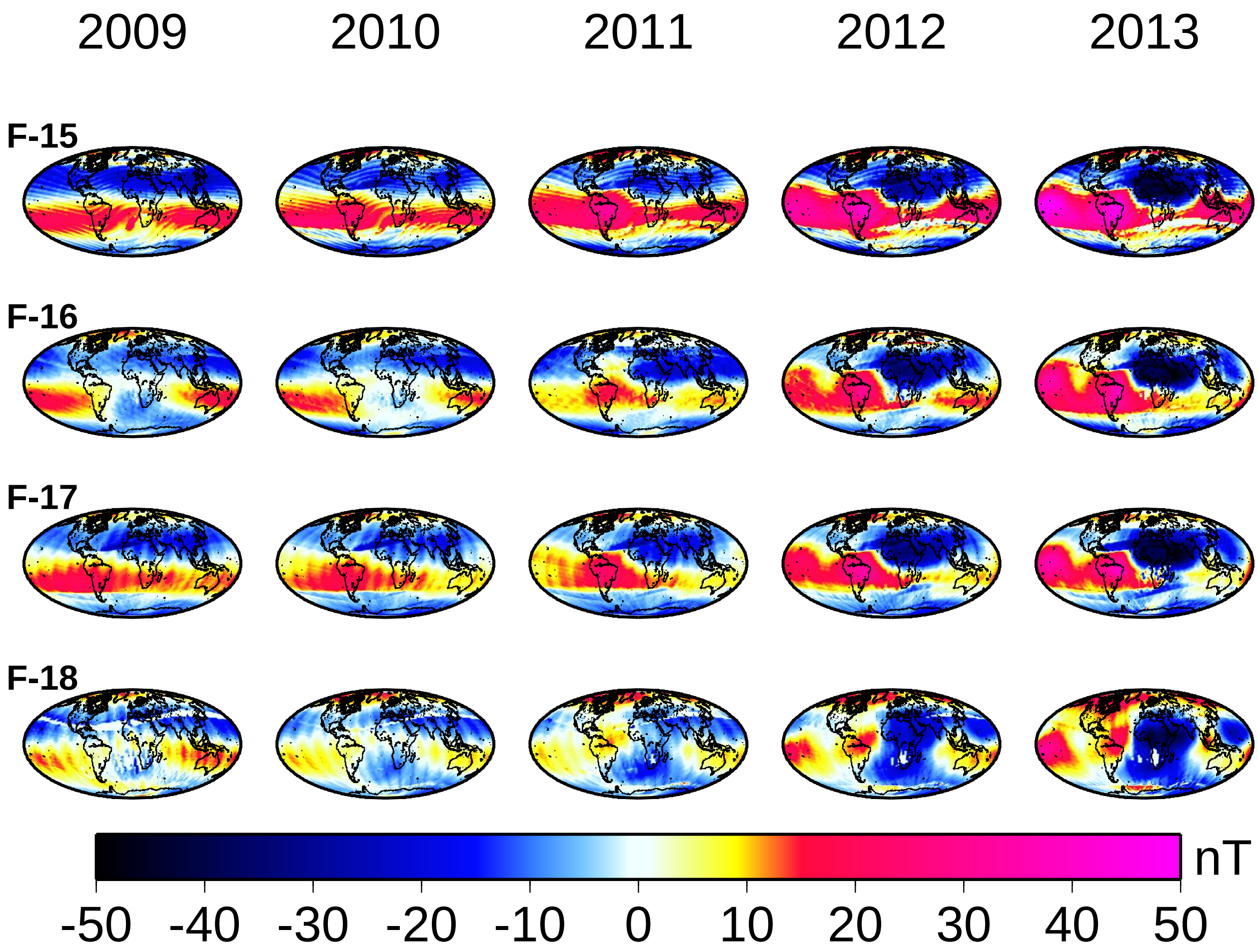

Figure 8. Calibrated B_z residuals for all satellites F-15 through F-18 and years 2009-2013.

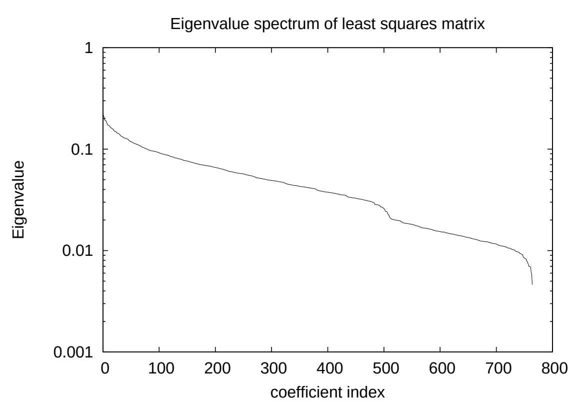

Figure 9. Eigenvalue spectrum of model least squares matrix as a function of coefficient index.

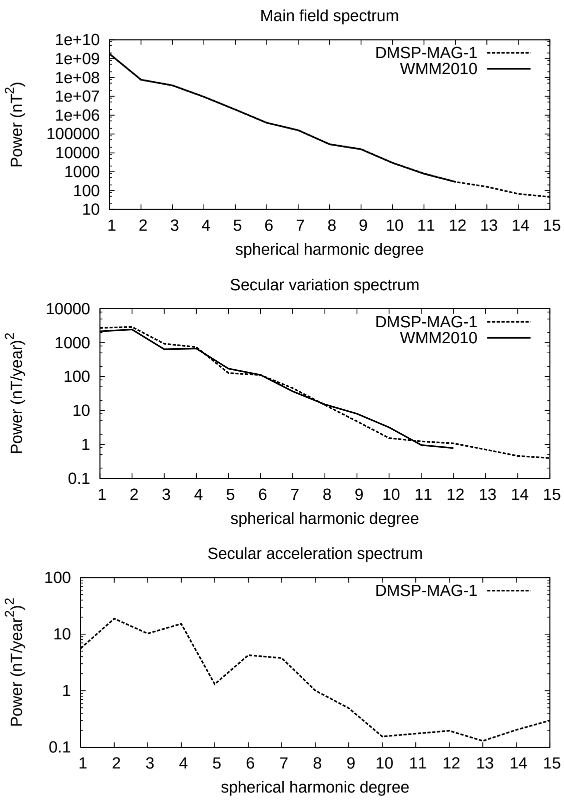

Figure 10. Main field, secular variation and secular acceleration coefficients of DMSP-MAG-1 compared with WMM2010 (WMM2010 does not provide secular acceleration).

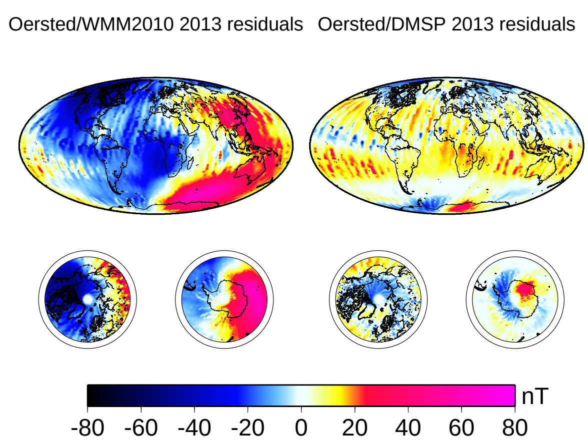

Figure 11. Residuals of Ørsted scalar data with WMM2010 (left) and DMSP-MAG-1 (right) from January through June 2013.